Journal of Materials Chemistry A

PAPER

View Article Online
View Journal | View Issue

Cite this: J. Mater. Chem. A, 2014, 2, 20980

Improving the thermoelectric performance of TiNiSn half-Heusler *via* incorporating submicron lamellae eutectic phase of $Ti_{70.5}Fe_{29.5}$: a new strategy for enhancing the power factor and reducing the thermal conductivity

A. Bhardwaj and D. K. Misra*

Received 9th September 2014
Accepted 30th October 2014

DOI: 10.1039/c4ta04661g

www.rsc.org/MaterialsA

The concept of a composite derived by incorporating a second minor phase in bulk thermoelectric materials has established itself as an effective paradigm for optimizing high thermoelectric performance. In this work, the incorporation of submicron lamellae eutectic phases into cheap, abundant and non-toxic TiNiSn half-Heusler is extended for the first time to optimize its thermoelectric performance. Half-Heusler (HH) TiNiSn/eutectic $Ti_{70.5}Fe_{29.5}$ composites were fabricated by employing the arc-melting route, followed by the spark plasma sintering (SPS) technique. Incorporating the metallic submicron lamellae eutectic phase of $Ti_{70.5}Fe_{29.5}$ into the HH TiNiSn matrix results in a substantial increase in the power factor (~57% higher than TiNiSn HH) and simultaneous reduction (~25% lower than TiNiSn HH) in the thermal conductivity, leading to an enhanced thermoelectric figure-of-merit (ZT) of 0.41 at 773 K for the half-Heusler (HH) TiNiSn/eutectic $Ti_{70.5}Fe_{29.5}$ composite with a mass ratio a 33 : 1, which is 105% higher than its counterpart TiNiSn HH. This enhancement in power factor is primarily due to an increase in electrical conductivity, resulting from the inclusion of the metallic $Ti_{70.5}Fe_{29.5}$ eutectic phase, while the reduction in thermal conductivity can be ascribed to the enhanced phonon scattering by numerous lamellae interfaces of β-Ti and TiFe of the eutectic phase and also their interfaces with the HH phase. The effective value of the thermal conductivity of HH TiNiSn/eutectic $Ti_{70.5}Fe_{29.5}$ composites, calculated by the effective medium theory in the light of Maxwell–Eucken approximations, matches well with the experimental value of thermal conductivity.

1. Introduction

The prospects of climate change, eventual fossil fuel depletion and an increasingly severe CO_2 problem have revived tremendous interest in exploring thermoelectric materials with high efficiency and thermoelectric technology. The efficiency of thermoelectric materials is gauged by the dimensionless thermoelectric figure of merit $ZT = \frac{\alpha^2 \sigma T}{\kappa}$, where σ is the electrical conductivity, α the Seebeck coefficient, κ the thermal conductivity and T the absolute temperature. The figure-of-merit requires a high Seebeck coefficient α, large electric conductivity σ, and low thermal conductivity κ.[1]

In past decades, several concepts, such as phonon-glass electron-crystal, (PGEC), heavy rattling atoms as phonon absorbers, high density of states at the Fermi energy, differential temperature dependence of density of states, high effective electron mass, superlattice structures and electron-phonon coupling have been established to design thermoelectric materials with optimized thermoelectric figures of merit. Based on these concepts, many materials such as Bi_2Te_3,[2] $AgPb_mSbTe_{2+m}$ (LAST),[3] TeAgGeSb (TAGS),[4] PbTe,[5] SiGe[6] Skutterudites[7] and Zintl phase compounds[8] have been widely investigated with their high ZT. Unfortunately, despite their high ZT, particularly state-of-the-art materials such as LAST[7] and TAGS[8] were associated with a major issue of low earth crust abundance and high market price of at least one of their components.

Among several thermoelectric materials developed so far for power generation, half-Heusler compounds (with general compositions MNiSn (n-type) and MCoSb (p-type), where M = Zr, Hf, Ti) are more environmentally benign, and are hence continually attracting tremendous interest in thermoelectric materials applications.[9] These compounds are generally semiconductors with narrow band-gaps. They usually show non-parabolic band features near the Fermi level. These combined features of narrow band gap and non-parabolic band facilitate a high thermoelectric power-factor PF ($=\alpha^2\sigma$) leading to high

CSIR-Network of Institutes for Solar Energy, Materials Physics & Engineering Division, CSIR-National Physical Laboratory, Dr. K. S. Krishnan Marg, New Delhi-110012, India. E-mail: misradk@nplindia.org; dakkmisra@gmail.com

ZT >1 in several state-of-the-art p-[10] and n-[11] type half-Heusler materials, which makes them a compatible module for thermoelectric devices. However, most of these half-Heusler state-of-the-art materials are doped with expensive and heavy elements. In this series of materials, TiNiSn-based materials are promising thermoelectric materials with regard to elemental abundance, since they contain earth-abundant and non-toxic elements, such as Ti and Sn.[12–14] They are easy to prepare in large quantities using conventional solid state synthesis. The drawback associated with these materials is extremely low value of ZT ($= (PF/\kappa) \times T$), which is primarily because of their very large thermal conductivities (κ) in comparison to the other state-of-the-art TE materials.

Many techniques, such as solid solution alloying,[15–19] nanostructuring,[20] and the investigation of new structures,[21,22] have been widely employed to disrupt the heat carrying phonons in order to overcome the large thermal conductivity for increasing ZT of this class of compounds. For applications at high temperatures, where materials for power generation are needed, the majority of phonons are most effectively scattered by features on the nanoscale and therefore significant reductions in thermal conductivities were noted, optimizing the high figure of merit of several thermoelectric materials.[10a,11b,e,23–28]

Nanostructuring, particularly *via* the nanocomposite approach in thermoelectric materials, has been demonstrated as an effective strategy for improving ZT by significantly reducing thermal conductivity while leaving the electronic properties either unaffected or improved in the process. The incorporation of particles such as ZrO_2,[29–31] Al_2O_3,[32] WO_3,[33] C_{60},[34] NiO[35] and HfO_2[36] into the matrix of HH thermoelectric materials has been documented very well as an efficient top-down approach to improve ZT. In such investigations it has been deduced that the increased phonon scattering by the interface between particles and the matrix leads to significant reduction in the thermal conductivity.

Apart from this strategy of fabricating composites by incorporation of a minor phase into a matrix phase, bulk thermoelectric composites may also be derived *via* spontaneous partitioning of a precursor phase into thermodynamically stable phases, which is also an exciting path to fabricate composite materials.[37–43] The use of such a microstructure to reduce thermal conductivity in thermoelectric materials has also been investigated.[42–44] The partitioning of quenched metastable phases into eutectic composite phases during a controlled process has also been well studied by Wu *et al.*,[45] to reveal fine microstructure for enhancing the thermoelectric performance. Such eutectic composite materials can be rapidly prepared and can even possibly reduce thermal conductivity.[42–45] In fact, a number of eutectic materials based on III–V and IV–VI compound semiconductors have been studied previously as thermoelectric materials with high ZT, due to reduced thermal conductivity.[40,43,46–51] In this direction of further reducing the thermal conductivity, metallic lamellae eutectic materials can be utilized by inclusion in the thermoelectric matrix, in order to improve the thermoelectric performance. Out of several metallic eutectic alloys, eutectic $Ti_{70.5}Fe_{29.5}$ is a low cost potential lightweight engineering material for industrial applications due to its excellent mechanical properties with yield strength ~1000 MPa, fracture strength (~2000–2600 MPa) and larger plasticity (>2%).[52,53] Moreover, its incorporation can increase the carrier concentration, which may increase the electrical conductivity, and the partially aligned lamellae of the β-Ti and TiFe interfaces may enhance the additional phonon scattering for further reduction of the thermal conductivity of these composites.

Herein we incorporate lamellae eutectic $Ti_{70.5}Fe_{29.5}$ phase into HH TiNiSn thermoelectric matrix to improve its ZT. We believe that it is highly possible that metallic submicron lamellae eutectic inclusions will lead to reduced κ, due to numerous interfaces for phonon scattering, together with large σ due to metallic inclusions, which will perhaps further improve the thermoelectric properties. To the best of our knowledge the incorporation of the eutectic phase into thermoelectric materials in order to study its effect on the thermoelectric properties has seldom been reported before. In this work, we investigate the effect of metallic eutectic inclusions into cheap, non-toxic, environmentally friendly and potentially thermoelectric matrix of HH TiNiSn on its thermoelectric properties. The electrically conductive eutectic $Ti_{70.5}Fe_{29.5}$, which is highly stable, was prepared by the arc melting method described in our previous reports.[53,54] A reduced value of κ was realized, due to the enhanced phonon scattering by numerous submicron lamellae interfaces of β-Ti and TiFe eutectic phases and grain boundaries. In conjunction with a reduction in thermal conductivity, the power factor is also increased due to enhanced electrical conductivity, leading to an improvement in ZT of 0.41 at 773 K for the half-Heusler (HH) TiNiSn/eutectic $Ti_{70.5}Fe_{29.5}$ composite with a mass ratio of 33 : 1.

2. Experimental details

2.1 Materials processing

TiNiSn (HH) and $Ti_{70.5}Fe_{29.5}$ were synthesized by direct arc-melting of titanium (Ti; 99.99%, Alfa Aesar, powder), nickel (Ni; 99.99%, Alfa Aesar, powder), tin (Sn; 99.99%, Alfa Aesar powder) and iron (Fe; 99.99%, Alfa Aesar, powder) in stoichiometric composition of TiNiSn and $Ti_{70.5}Fe_{29.5}$. For synthesis of the TiNiSn compound, the Sn was placed on top of Ti and Ni, which were initially melted, then the molten Sn diffused into the (Ti and Ni) matrix. The resulted TiNiSn melted ingot was then annealed at 1073 K for one week under vacuum in a quartz tube, which helps to accelerate atomic diffusion throughout the matrix for stabilization of the phases, to achieve a homogeneous phase. Both ingots were then broken into small pieces and grounded to a very fine powder using a mortar and pestle. The TiNiSn half-Heusler and eutectic $Ti_{70.5}Fe_{29.5}$ powders were mixed together in different mass ratios of 100 : 1, 33 : 1 and 20 : 1, employing planetary high energy ball milling to obtain a homogeneous and well-distributed mixture. These mixtures were consolidated by employing spark plasma sintering (SPS) at a temperature of 1073 K and a pressure of 50 MPa for a holding time of 10 minutes, using a graphite die of 12.7 mm diameter to get 12.7 mm diameter bulk dense pellets. The obtained samples were cut into two pieces, one in the form of a bar about 3 × 2 ×

10 mm^3 and the other into 12.7 mm diameter discs, which were used for measuring the electronic and thermal transport.

2.2 Powder X-ray diffraction

The gross structural characterization of half-Heusler (HH) TiNiSn/eutectic $Ti_{70.5}Fe_{29.5}$ composites was carried out by powder X-ray diffractometer (Rigaku Mini Flex II) in reflection $\theta - 2\theta$ geometry, with a position sensitive detector (Ultafast D Tex), operating at 30 kV and 20 mA, using a graphite monochromator and CuK_{α} radiation with wavelength $\lambda \approx 1.5406$Å along with a $CuK_{\alpha 2}$ filter and rotating anode equipped with a powder 2θ diffractometer ranging from 20 to 80 degrees. The experimental conditions and parameters such as sample size, power ratings of X-ray tube (30 kV, 20 mA) and other diffractometer parameters such as scan speed, counting steps *etc.* were kept constant for all the diffraction experiments.

2.3 Electron microscopy

The microstructure investigation of the host TiNiSn HH compound and the HH TiNiSn/eutectic $Ti_{70.5}Fe_{29.5}$ composite with mass ratio 33 : 1 was carried out by field emission scanning electron microscopy (FE-SEM; model: SUPRA40 VP, operating at 30 kV) and HRTEM (model: Technai G^2F^{30}; STWIN) operating at 300 kV. The TEM specimens were prepared in three steps. Initially, the SPS processed pellets were cut into 3 mm discs using an ultrasonic disc cutter (model: Gaton 170). The specimen was then mechanically polished with a load of 15 g using a dimple grinder (model: South Bay Technology 515) and finally an electron transparent specimen for TEM analysis was achieved by Ar^+-ion milling (model: Boltech RES 101). Elemental analysis of the samples was performed using energy dispersive spectroscopy (EDS) attached to the FE-SEM.

2.4 Thermoelectric properties

Thermal diffusivity of HH TiNiSn/eutectic $Ti_{70.5}Fe_{29.5}$ composites (with mass ratios of HH : $Ti_{70.5}Fe_{29.5}$ to 100 : 1, 33 : 1, 20 : 1) samples were measured using a laser flash system (Linseis, LFA 1000) on disk-shaped specimens with an approximate thickness of 2.0 mm and diameter 12.7 mm. The disc specimens used for thermal diffusivity were sprayed with a layer of graphite in order to minimize errors due to emissivity. The specific heat was determined by a Differential scanning calorimetry (DSC) instrument (822e Mettler Toledo). The thermal conductivity of the composites was calculated using the relation, $\kappa = d \times C_p \times \rho$, where d is the thermal diffusivity, ρ, the geometrical pellet density and C_p, the heat capacity. The Seebeck coefficient and resistivity were measured simultaneously, employing commercial equipment (ULVAC, ZEM3) over the temperature range 300–773 K on samples of polished bars of about $3 \times 2 \times 10$ mm^3.

3. Results and discussion

3.1 X-ray diffraction analysis

The powder XRD patterns of TiNiSn, $Ti_{70.5}Fe_{29.5}$ and HH TiNiSn/eutectic $Ti_{70.5}Fe_{29.5}$ composite with mass ratio of 33 : 1 are shown in Fig. 1(a) & (b). The XRD patterns were indexed and the cell constants were refined by the POLSQ FORTRAN program.[55] Fig. 1(a) shows the XRD pattern of the TiNiSn HH sample. All the peaks in the XRD pattern (Fig. 1(a)) are well indexed with the cubic crystal system (space group $F\bar{4}3m$; no. 216) based on JCPDS card no. 00-023-1281, although it has been noted in several reports that unreacted elements and intermetallic compounds are usually precipitated due to incongruent melting of the TiNiSn system.[28,58,60] However, we are not able to detect such impurities in the background of XRD and electron microscopy investigations. The absence of such impurities could be due the precautions taken during the synthesis procedure, combined with arc-melting and long annealing time, as described in the experimental section. The lattice parameter was computed to be $0.594 \pm 0.513 \times 10^{-4}$ nm using POLSQ FORTRAN program.[55] The unit cell of TiNiSn is shown in the inset of Fig. 1(a). Fig. 1(b) presents the XRD pattern of the $Ti_{70.5}Fe_{29.5}$ eutectic phase and the HH TiNiSn/eutectic $Ti_{70.5}Fe_{29.5}$ composite with mass ratio 33 : 1. All the peaks observed for $Ti_{70.5}Fe_{29.5}$ are well matched with the β-Ti (space group $Im\bar{3}m$; no. 229) phase and the TiFe (space group $Pm3m$; no. 221) phase of the $Ti_{70.5}Fe_{29.5}$ eutectic alloy. The lattice parameter of the β-Ti solid solution, $a = 0.318 \pm 0.513 \times 10^{-4}$ nm in the $Ti_{70.5}Fe_{29.5}$ alloy was considerably smaller than that of pure β-Ti (0.3307 nm), owing to the dissolution of Fe, while the lattice parameter of the TiFe phase was $0.299 \pm 0.614 \times 10^{-4}$ nm in the $Ti_{70.5}Fe_{29.5}$ alloy; this was larger than that for the equiatomic FeTi phase (0.2975 nm) owing to the dissolution of Ti, similarly to our earlier report.[53,54] The standard patterns for pure β-Ti and TiFe phase reflections are also shown in Fig. 1(b) for comparison of the observed XRD patterns. The XRD pattern of the HH TiNiSn/eutectic $Ti_{70.5}Fe_{29.5}$ composite with mass ratio 33 : 1 (Fig. 1(b)) reveals the major prominent peaks corresponding to HH only; no evident peaks corresponding to the β-Ti and TiFe phases of the $Ti_{70.5}Fe_{29.5}$ eutectic alloy were noticed, which could be due to the small amount of eutectic $Ti_{70.5}Fe_{29.5}$ inclusions to strongly diffracted X-ray radiation.

3.2 Scanning and transmission electron microscopy

In order to further identify the phases and microstructural details, SEM and TEM for TiNiSn, $Ti_{70.5}Fe_{29.5}$ and the HH TiNiSn/eutectic $Ti_{70.5}Fe_{29.5}$ composite with mass ratio 33 : 1 have been carried out. The SEM morphology of the TiNiSn sample clearly reveals a single phase contrast as shown in Fig. 2(a). The EDAX analysis (Fig. 2(b)) confirms this sample as a pure TiNiSn half-Heusler phase, which is also consistent with the XRD analysis. Fig. 2(c) presents the SEM morphology obtained from the sample of eutectic $Ti_{70.5}Fe_{29.5}$ alloy, displaying alternating bright and dark phases, which is a typical feature of the eutectic microstructure. These lamellae are confirmed as β-Ti (A2) and FeTi (B2) by EDAX analysis, as marked in Fig. 2(d). Interestingly, one can observe that the eutectic colonies grow (Fig. 2(d)) by forming sharp eutectic cell boundaries, similarly to our earlier report.[53] The eutectic spacing was observed to be in range 600–1200 nm. The widths of β-Ti (A2) and FeTi (B2) lamellae eutectic were noted to be in the range 400–800 nm and 300–700 nm, respectively, showing

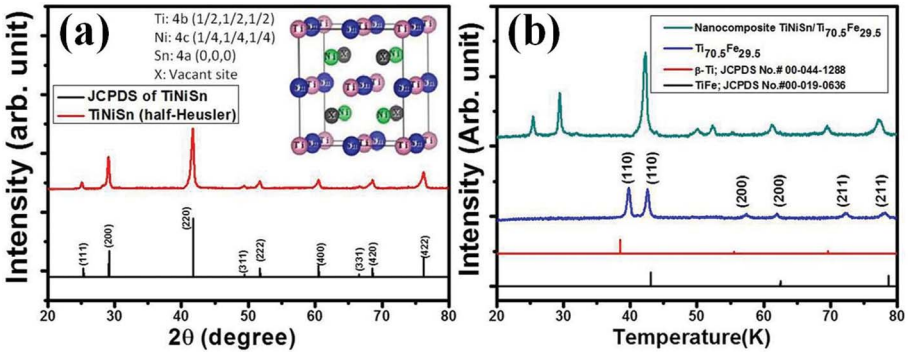

Fig. 1 (a) X-ray diffraction (XRD) pattern of TiNiSn HH and its JCPDS card no. 00-023-1281. The ball and stick arrangement for the half-Heusler (HH) structure illustrating the atomic arrangement is shown in the inset of (a). (b) XRD pattern of the $Ti_{70.5}Fe_{29.5}$ eutectic phase and the HH TiNiSn/eutectic $Ti_{70.5}Fe_{29.5}$ composites with mass ratio of 33 : 1.

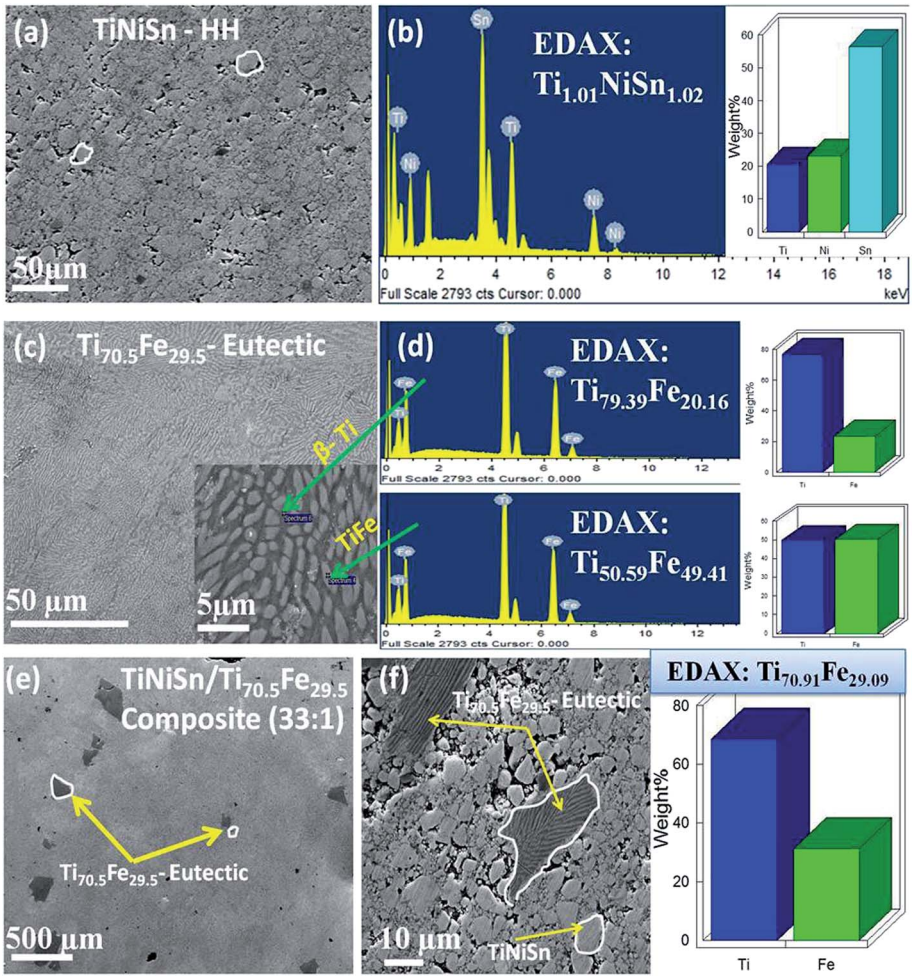

Fig. 2 (a) FE-SEM micrograph of the TiNiSn parent compound, showing a single phase contrast of the half-Heusler phase, (b) EDAX spectrum of TiNiSn showing qualitatively the presence of constituent elements Ti, Ni and Sn; the composition analysis confirms the composition to be very close to TiNiSn, (c) SEM image of the $Ti_{70.5}Fe_{29.5}$ eutectic phase showing alternating bright and dark phase contrasts, which are more clearly visible in the inset of (c), (d) EDAX spectra obtained from these alternating lamellae as marked in (c) confirming the presence of β-Ti and TiFe phases of the eutectic $Ti_{70.5}Fe_{29.5}$ alloy, (e) SEM morphology of the HH TiNiSn/eutectic $Ti_{70.5}Fe_{29.5}$ composite with a mass ratio of 33 : 1 revealing the two phase contrast mixture, (g) magnified image of HH TiNiSn/eutectic $Ti_{70.5}Fe_{29.5}$ composite showing clear eutectic features in the HH matrix. The composition of the eutectic alloy was confirmed by EDAX analysis.

the submicron level features of the lamellae eutectic phase. Fig. 2(e) shows the SEM morphology of the HH TiNiSn/eutectic $Ti_{70.5}Fe_{29.5}$ composite with mass ratio of 33 : 1, revealing the two phase mixture. For better resolution of the eutectic features in the composite sample, Fig. 2(e) was further magnified and a clear lamellae eutectic feature can be seen in Fig. 2(f). The exact composition of the eutectic is confirmed by EDAX analysis, which is presented in Fig. 2(f).

Transmission electron microscopy of TiNiSn HH and the HH TiNiSn/eutectic $Ti_{70.5}Fe_{29.5}$ composite with mass ratio 33 : 1 has been carried out to see the microstructure and their internal structure. Fig. 3(a) displays a bright field electron micrograph corresponding to TiNiSn HH, showing grains with sizes ranging from 0.1 μm to 8 μm. The selected area electron diffraction (SAED) corresponding to one of the grains presents the HH phase with zone axis [1$\bar{1}$1]. The bright field TEM image of the TiNiSn HH/$Ti_{70.5}Fe_{29.5}$ eutectic composite with mass ratio 33 : 1 is presented in Fig. 3(c) showing two phase contrasts, one with eutectic features (marked by the dotted area) and HH as the matrix phase. An obvious representative image of the eutectic feature is presented in the inset of Fig. 3(c). The SAED pattern taken from the eutectic feature as shown in Fig. 3(d) confirms it to be β-Ti and TiFe of the eutectic phase. Despite looking at the nature of the grain boundary interface in the TEM image at HRTEM mode, we could not discern atomic scale resolution features of the grain boundary interface, either due to thick samples or due to the lower instrumental resolution to detect such minor features.

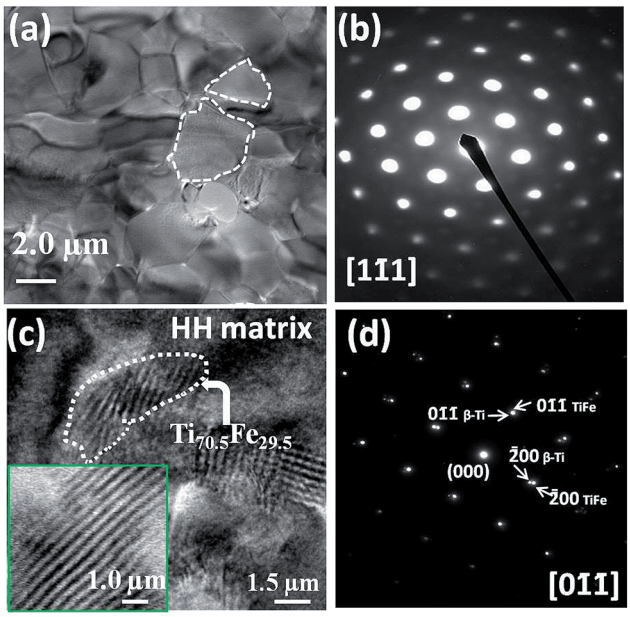

Fig. 3 (a) TEM image obtained from the specimen of TiNiSn presenting highly densified grains, (b) SAED pattern corresponding to the TiNiSn HH phase with zone axis [1$\bar{1}$1], (c) TEM image of the HH TiNiSn/eutectic $Ti_{70.5}Fe_{29.5}$ composite with mass ratio 33 : 1 showing two phase contrasts, one with eutectic features (marked by the dotted area) and HH as the matrix phase. A representative image of the eutectic feature is presented in the inset of (c), (d) The SAED pattern taken from the eutectic feature confirms the β-Ti and TiFe of the eutectic phase.

3.3 Electronic and thermal transport properties

The electronic and thermal transport properties of all the composites have been compared with the parent TiNiSn (HH) material. Fig. 4(a) shows the temperature dependence of electrical conductivity (σ), of the HH TiNiSn/eutectic $Ti_{70.5}Fe_{29.5}$

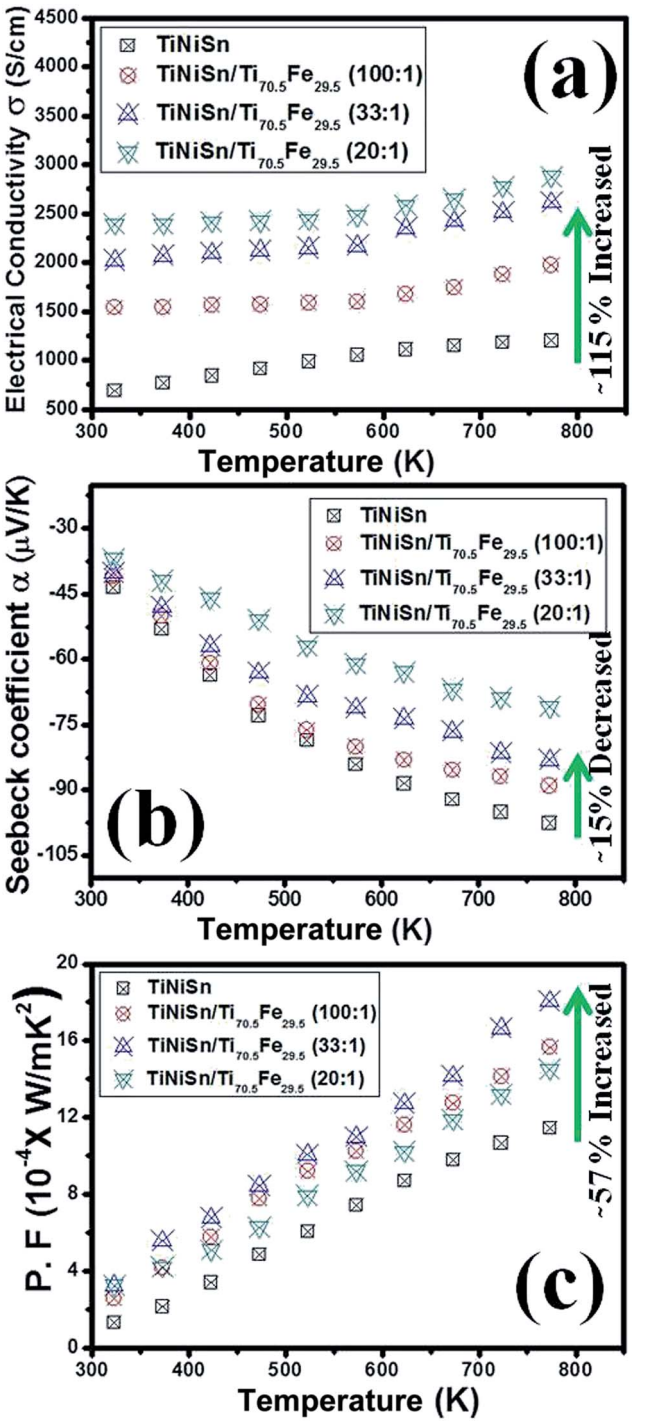

Fig. 4 (a) Temperature dependence of (a) the electrical conductivity σ (T), (b) the Seebeck coefficient, α (T), (c) power factor, $\sigma\alpha^2(T)$ of bare TiNiSn (HH) and HH TiNiSn/eutectic $Ti_{70.5}Fe_{29.5}$ composites with different mass ratios of 100 : 1, 33 : 1 and 20 : 1.

composites for different mass ratios. Regardless of the temperature, the electrical conductivity increases with increasing $Ti_{70.5}Fe_{29.5}$ eutectic phase concentration and reaches its maximum value for the composite with mass ratio 20 : 1. With increasing temperature, the σ (T) also increases for all the composite samples. However, the temperature dependent behavior is not strongly dominating, showing that the composites are highly doped degenerate semiconducting materials. The room temperature measurements of the Hall coefficient (R_H) were used to determine a Hall carrier concentration ($n = 1/R_H e$) for all composites. Interestingly, the carrier concentration at room temperature increases with increasing concentration of the metallic $Ti_{70.5}Fe_{29.5}$ eutectic phase. Further, the room temperature electrical conductivity and carrier concentration n are used to calculate the room temperature mobility (μ) by a relation $\sigma = ne\mu$ (where n is the carrier concentration, e is the charge of an electron and μ is the carrier mobility) and the results are shown in Table 1. In light of the room temperature Hall data, we may infer that the increased electrical conductivity of the HH TiNiSn/eutectic $Ti_{70.5}Fe_{29.5}$ composites is ascribed to the increase in carrier concentration induced by incorporating the metallic $Ti_{70.5}Fe_{29.5}$ eutectic phase into the HH matrix. We also noticed that the electron mobility of the composites increases with increasing metallic inclusions. We, therefore, reasonably believe that the partially aligned lamellae of β-Ti and TiFe of the $Ti_{70.5}Fe_{29.5}$ eutectic phase are most likely to provide a continuous electronic transport path, as evidenced by high electron mobility, which gives a higher electrical conductivity.

The temperature dependent Seebeck coefficients for bare TiNiSn (HH) and HH TiNiSn/eutectic $Ti_{70.5}Fe_{29.5}$ composites are shown in Fig 4(b). The Seebeck coefficients of all the samples are large and negative, indicating that electrons are the majority carriers in these samples (n-type). Interestingly, the associated decrease in Seebeck coefficients observed for all the composites at room temperature is consistent with increased electrical conductivity. This phenomenon of an inverse relation between α and σ can be explained by the equation,[56]

$$\alpha = \pm\frac{k_B}{e}\left[2 + \ln\frac{2(2\pi m^* k_B T)^{3/2}}{h^3 n}\right] \quad (1)$$

where m^* is the effective mass relating the density of states and n, the carrier concentration. As noted above, the introduction of the metallic $Ti_{70.5}Fe_{29.5}$ eutectic phase induces large carrier concentration and hence, according to the equation, α is reduced.

The temperature dependent Seebeck coefficient of all the composite samples increases with temperature up to 773 K, similar to the increase in electrical conductivity with rising temperature. Usually in a semiconductor the simultaneous increase in σ and α is not expected and would require a high temperature Hall measurement for better understanding.

Fig. 4(c) displays the power factor ($PF = \alpha^2\sigma$) of matrix TiNiSn (HH) and HH TiNiSn/eutectic $Ti_{70.5}Fe_{29.5}$ composites. Interestingly, all the composites except the HH TiNiSn/eutectic $Ti_{70.5}Fe_{29.5}$ composite with mass ratio 20 : 1 exhibit a higher power factor compared to the matrix TiNiSn (HH), which is mainly ascribed to the increased σ. We noticed a small decrease in α and that is compensated by this large increase in σ to achieve the large power factor. The highest power factor of 18.05×10^{-4} W m^{-1} K^{-2} at 773 K was optimized for the HH TiNiSn/eutectic $Ti_{70.5}Fe_{29.5}$ composite with mass ratio 33 : 1, which is ~57% larger than the bare TiNiSn ($PF = 11.43 \times 10^{-4}$ W m^{-1} K^{-2}).

Fig. 5(a) displays the temperature dependence of the total thermal conductivity κ (T) of bare TiNiSn (HH) and the HH TiNiSn/eutectic $Ti_{70.5}Fe_{29.5}$ composites. Regardless of the temperature, the total thermal conductivity decreases with increasing concentration of the metallic submicron lamellae eutectic $Ti_{70.5}Fe_{29.5}$ phase in the TiNiSn (HH) thermoelectric matrix. With increasing temperature, the total thermal conductivity, κ, also decreases, indicating that phonon conductivity is dominating. Interestingly, the TiNiSn HH/$Ti_{70.5}Fe_{29.5}$ composites with mass ratio 33 : 1 displayed a low thermal conductivity (~3.42 W m^{-1} K^{-1}) at 773 K, which is 25% lower than the bare TiNiSn. The reduction in thermal conductivity can be ascribed by the enhanced phonon scattering by numerous submicron lamellae interfaces of the β-Ti and TiFe eutectic phase and also by grain boundaries. We conclude that the incorporation of submicron lamellae of β-Ti and TiFe of the $Ti_{70.5}Fe_{29.5}$ eutectic phase, with interface spacing less than 1200 nm, facilitates enhancement of the scattering of phonons in the present case, most possibly similar to an earlier observation reported by Wu *et al.*[45] in Ag–Pb–Te materials. However, the exact mechanism of effective phonon scattering with long to short mean path to significantly reduce the thermal conductivity in such HH TiNiSn/eutectic $Ti_{70.5}Fe_{29.5}$ composites, is not clear at this stage and would require further study. The effective values of thermal conductivities of the HH TiNiSn/eutectic $Ti_{70.5}Fe_{29.5}$ composites were also calculated, assuming TiNiSn as the HH matrix and $Ti_{70.5}Fe_{29.5}$ eutectic as the inclusion by using the effective medium theory in the light of Maxwell–Eucken (eqn (2)) approximations,[57]

Table 1 Hall measurement data of half-Heusler (HH) TiNiSn/eutectic $Ti_{70.5}Fe_{29.5}$ nanocomposites at room temperature

Nominal composition	Hall coefficient (R_H) × 10^{-2} cm^3 C^{-1}	Carrier conc. n (10^{19} cm^{-3})	Mobility μ (cm^2 V^{-1} s^{-1})
TiNiSn	10.5	5.9	121
TiNiSn/$Ti_{70.5}Fe_{29.5}$ (100 : 1)	6.7	9.3	127
TiNiSn/$Ti_{70.5}Fe_{29.5}$ (33 : 1)	6.3	9.8	159
TiNiSn/$Ti_{70.5}Fe_{29.5}$ (20 : 1)	5.8	10.3	167

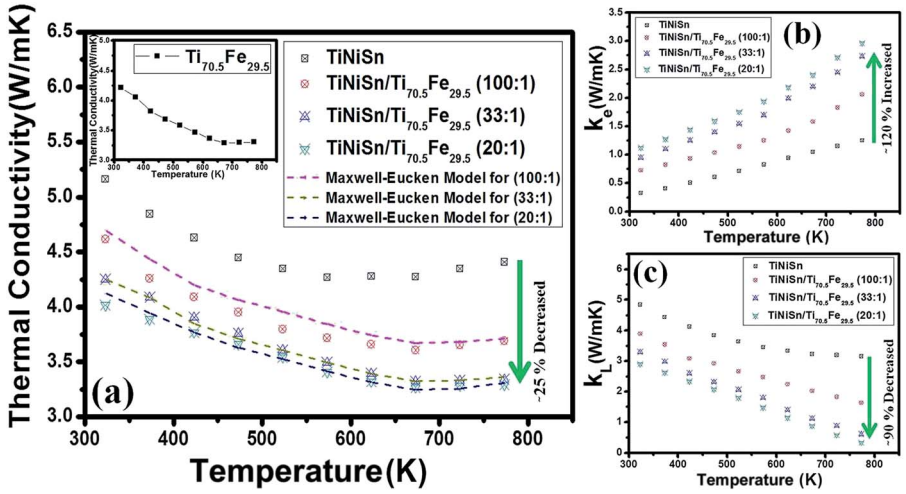

Fig. 5 (a) Temperature dependence behavior of the total thermal conductivity κ (T) of bare TiNiSn (HH) and HH TiNiSn/eutectic $Ti_{70.5}Fe_{29.5}$ composites with different mass ratios of 100 : 1, 33 : 1 and 20 : 1 with calculated effective thermal conductivity for all the composites using the effective medium theory and Maxwell–Eucken approximations; inset of (a) shows the total thermal conductivity of eutectic $Ti_{70.5}Fe_{29.5}$. (b) The electronic and (c) lattice thermal conductivity of bare TiNiSn (HH) and HH TiNiSn/eutectic $Ti_{70.5}Fe_{29.5}$ composites with different mass ratios of 100 : 1, 33 : 1 and 20 : 1.

$$K = \frac{k_1 v_1 + k_2 v_2 \frac{3k_1}{2k_1 + k_2}}{v_1 + v_2 \frac{3k_1}{2k_1 + k_2}} \quad (2)$$

where K is the effective thermal conductivity of the composite, κ_1 = continuous phase *i.e.* the thermal conductivity of the matrix, κ_2 = dispersed phase *i.e.* thermal conductivity of the inclusion, and v_1 and v_2 are the volume fractions of the matrix and second phase, respectively. The value of κ_2, *i.e.* the thermal conductivity of the $Ti_{70.5}Fe_{29.5}$ eutectic inclusion, was taken from the data shown in the inset of Fig. 5(a).

Based on the model described above, the calculated thermal conductivity of all the composites presents a similar trend to the experimentally observed thermal conductivities of the composites with slight variations in their values, as shown by their corresponding line curves in Fig. 5(a). The slight deviation in the thermal conductivities may occur due to either the experimental error or the approximation limit of the model.

The lattice thermal conductivity was obtained by subtracting the electronic thermal conductivity from the total measured thermal conductivity. The Wiedemann–Franz law has been used to calculate the electronic thermal conductivity ($\kappa_e = L\sigma T$, where L is the Lorenz number, σ the electrical conductivity and T the temperature in K), which is shown in Fig. 5(b). Here, we use the temperature dependent Lorenz number calculated specifically for TiNiSn by Birkel *et al.*,[58] and the bipolar contribution was taken into account by assuming $\kappa_{lattice} \sim 1/T$.[59] Fig. 5(c) represents the temperature dependent lattice thermal conductivity. The lattice thermal conductivity of all the samples was observed to decrease with increasing temperature, showing a similar falling trend in the total thermal conductivity. The lattice thermal conductivity of TiNiSn half-Heusler at room temperature is approximately 5.0 W m^{-1} K^{-1}, which agrees well with the previously published results.[60] Thus, we notice that the lattice thermal conductivity significantly contributes to the total thermal conductivity, as envisaged from Fig 5 (b) and (c). Interestingly, a drastic reduction in the lattice thermal conductivity in the composite with mass ratio 33 : 1 was observed, which is attributed to the numerous lamellae interfaces in matrix, which disrupt the heat carrying phonons to lowering the lattice thermal conductivity. The temperature dependent lattice thermal conductivity shows a remarkable decrease $\kappa_l \approx$ 0.3 W m^{-1} K^{-1} at high temperature, which is attributed to the short range phonon scattering, due to the lamellae structure at high temperature in the HH matrix. Thus, such structural modification, by incorporating the lamellae eutectic inclusions, leads to the reduced lattice thermal conductivity, which is a significant reduction of more than 70% as compared to the lattice thermal conductivity of TiNiSn, the system with the highest ZT reported by Downie *et al.*[28]

3.4 Thermoelectric figure of merit

The temperature dependence of ZT of all the samples is calculated, as displayed in Fig. 6. The ZT of the HH TiNiSn/eutectic $Ti_{70.5}Fe_{29.5}$ composites increases with rising temperature. The maximum ZT $\approx$ 0.41 at a temperature of 773 K for the HH TiNiSn/eutectic $Ti_{70.5}Fe_{29.5}$ composite was optimized for the mass ratio 33 : 1, which is significantly enhanced as compared to ZT $\approx$ 0.20 at 773 K for bare TiNiSn. Thus, combining a large increase (~57%) in the power factor, due to significant enhancement of the electrical conductivity (~115%), along with a 25% reduction in the thermal conductivity, the ZT of the HH TiNiSn/eutectic $Ti_{70.5}Fe_{29.5}$ composite with mass ratio 33 : 1 was calculated to be about 105% larger than that of the bare TiNiSn sample.

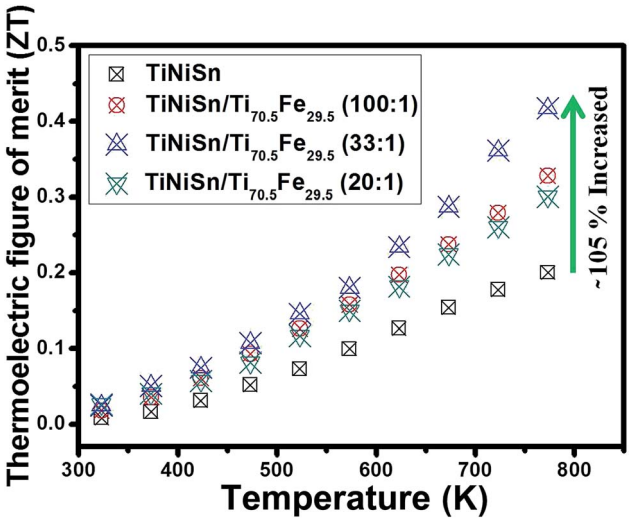

Fig. 6 Temperature dependence of the thermoelectric figure of merit of bare TiNiSn (HH) and HH TiNiSn/eutectic $Ti_{70.5}Fe_{29.5}$ composites, with different mass ratios of 100 : 1, 33 : 1 and 20 : 1.

4. Conclusion and future prospects

In summary, novel half-Heusler (HH) TiNiSn/eutectic $Ti_{70.5}Fe_{29.5}$ composites have been fabricated by incorporating metallic $Ti_{70.5}Fe_{29.5}$ eutectic alloy into pre-synthesized TiNiSn (HH) precursors using high energy mechanical ball milling and further consolidated by spark plasma sintering. A significant enhancement in the electrical conductivity (~115% larger value than bare TiNiSn) with moderate decrease in the Seebeck coefficient results in a large increase in power factor (~57% larger value than bare TiNiSn) of the HH TiNiSn/eutectic $Ti_{70.5}Fe_{29.5}$ composite with mass ratio 33 : 1. Moreover, despite the metallic nature of the lamellae eutectic $Ti_{70.5}Fe_{29.5}$, the thermal conductivity of this composite was also significantly decreased (~25% reduced value compared to bare TiNiSn). The drastic reduction in the thermal conductivity is attributed to a significant reduction in the lattice thermal conductivity due to effective phonon scattering, which arises from the submicron lamellae β-Ti and TiFe interfaces of the $Ti_{70.5}Fe_{29.5}$ eutectic phase and the numerous grain boundaries. A higher ZT of 0.41 at 773 K was obtained in the HH TiNiSn/eutectic $Ti_{70.5}Fe_{29.5}$ composite (mass ratio: 33 : 1), which is 105% larger than that of the normal TiNiSn half-Heusler. Such a significant increase in ZT is quite remarkable considering that only a small amount of $Ti_{70.5}Fe_{29.5}$ was introduced to form such an efficient composite. Relatively, earth abundance and non-toxicity of Ti, Ni, Sn and Fe involved in such a composite materials make them a cheap, alternative option and find widespread use as an alternative to the scarce and expensive Te and Pb used in the commercialized state-of-the-art thermoelectric materials. We strongly believe that the present strategy of fabricating such a composite by incorporating a submicron metallic lamellae eutectic in the TiNiSn half-Heusler may be a very effective and promising approach, and can be deployed not only for the TiNiSn half-Heusler but for most existing potential bulk thermoelectric materials to enhance their thermoelectric performance.

Acknowledgements

This work was supported by the CSIR-TAPSUN (NWP- 54) programme entitled "Novel approaches for solar energy conversion under technologies and products for solar energy utilization through networking". The authors are grateful to the Director, Prof. R. C. Budhani (Director, CSIR-NPL), for his constant mentoring and support for this project. The authors thank Dr A. M. Biradar (CSIR-NPL) and Dr Jiji Pullikotil (CSIR-NPL) for their continuous encouragement. We acknowledge Dr Sunil Pandey (NIMS University, Jaipur) for providing the room temperature Hall data. One of the authors AB greatly acknowledges UGC-CSIR for financial support. The technical support rendered by Mr Radhey Shyam and Mr Naval Kishor Upadhyay is gratefully acknowledged.

References

1 G. J. Snyder and E. S. Toberer, *Nat. Mater.*, 2008, **7**, 105.
2 (*a*) B. Poudel, Q. Hao, Y. Ma, Y. Lan, A. Minnich, B. Yu, X. Yan, D. Wang, A. Muto, D. Vashaee, X. Chen, J. Liu, M. S. Dresselhaus, G. Chen and Z. Ren, *Science*, 2008, **320**, 634; (*b*) S. Yu, J. Yang, Y. Wu, Z. Han, J. Lu, Y. Xie and Y. Qian, *J. Mater. Chem.*, 1998, **8**, 1949; (*c*) J. Shen, T. Zhu, X. Zhao, S. Zhang, S. Yanga and Z. Yina, *Energy Environ. Sci.*, 2010, **3**, 1519; (*d*) M. E. Anderson, S. S. N. Bharadwaya and R. E. Schaak, *J. Mater. Chem.*, 2010, **20**, 8362; (*e*) S. Sumithra, N. J. Takas, D. K. Misra, W. M. Nolting, P. F. P. Poudeu and K. L. Stokes, *Adv. Energy Mater.*, 2011, **1**, 1141.
3 K. F. Hsu, S. Loo, F. Guo, W. Chen, J. S. Dyck, C. Uher, T. Hogan, E. K. Polychroniadis and M. G. Kanatzidis, *Science*, 2004, **303**, 818.
4 J. Androulakis, K. F. Hsu, R. Pcionek, H. Kong, C. Uher, J. J. D'Angelo, A. Downey, T. Hogan and M. G. Kanatzidis, *Adv. Mater.*, 2006, **18**, 1170.
5 (*a*) J. R. Sootsman, H. Kong, C. Uher, J. J. D'Angelo, C. I. Wu, T. P. Hogan, T. Caillat and M. G. Kanatzidis, *Angew. Chem., Int. Ed.*, 2008, **47**, 8618; (*b*) K. Ahn, K. Biswas, J. He, I. Chung, V. Dravid and M. G. Kanatzidis, *Energy Environ. Sci.*, 2013, **6**, 1529.
6 R. Basu, S. Bhattacharya, R. Bhatt, M. Roy, S. Ahmad, A. Singh, M. Navaneethan, Y. Hayakawa, D. K. Aswal and S. K. Gupta, *J. Mater. Chem. A*, 2014, **2**, 6922.
7 (*a*) G. Rogl, A. Grytsiv, P. Rogl, E. Bauer, M. Hochenhofer and E. Schafler, *Acta Mater.*, 2014, **76**, 434–438; (*b*) B. C. Sales, D. Mandrus and R. K. Williams, *Science*, 1996, **272**, 1325; (*c*) R. C. Mallik, R. Anbalagan, G. Rogl, E. Royanian, P. Heinrich, E. Bauer, P. Rogl and S. Suwas, *Acta Mater.*, 2013, **61**, 6698–6711; (*d*) R. C. Mallik, R. Anbalagan, K. K. Raut, A. Bali, E. Royanian, E. Bauer, G. Rogl and P. Rogl, *J. Phys.: Condens. Matter*, 2013, **25**, 105701; (*e*) E. Bauer, St. Berger, Ch. Paul, M. Della Mea, G. Hilscher,

H. Michor, M. Reissner, W. Steiner, A. Grytsiv, P. Rogl and E. W. Scheidt, *Phys. Rev. B: Condens. Matter*, 2002, **66**, 214421; (*f*) L. Zhang, A. Grytsiv, P. Rogl, E. Bauer and M. Zehetbauer, *J. Phys. D: Appl. Phys.*, 2009, **42**, 225405; (*g*) A. Grytsiv, P. Rogl, St. Berger, Ch. Paul, E. Bauer, C. Godart, B. Ni, M. M. Abd-Elmeguid, A. Saccone, R. Ferro and D. Kaczorowski, *Phys. Rev. B: Condens. Matter*, 2002, **66**, 094411; (*h*) J. W. Graff, X. Zeng, A. M. Dehkordi, J. He and T. M. Tritt, *J. Mater. Chem. A*, 2014, **2**, 8933–8940; (*i*) G. Rogl, A. Grytsiv, P. Rogl, N. Peranio, E. Bauer, M. Zehetbauer and O. Eibl, *Acta Mater.*, 2014, **63**, 30–43.

8 (*a*) A. Bhardwaj and D. K. Misra, *RSC Adv.*, 2014, **4**, 34552; (*b*) G. J. Snyder, M. Christensen, E. Nishibori, T. Caillat and B. B. Iversen, *Nat. Mater.*, 2004, **3**, 458; (*c*) S. R. Brown, S. M. Kauzlarich, F. Gascoin and G. J. Snyder, *Chem. Mater.*, 2006, **18**, 1873; (*d*) A. Bhardwaj, A. Rajput, A. K. Shukla, J. J. Pulikkotil, A. K. Srivastava, A. Dhar, G. Gupta, S. Auluck, D. K. Misra and R. C. Budhani, *RSC Adv.*, 2013, **3**, 8504; (*e*) S. K. Bux, A. Zevalkink, O. Janka, D. Uhl, S. Kauzlarich, J. G. Snyder and J. P. Fleurial, *J. Mater. Chem. A*, 2014, **2**, 215; (*f*) N. Kazem, W. Xie, S. Ohno, A. Zevalkink, G. J. Miller, G. J. Snyder and S. M. Kauzlarich, *Chem. Mater.*, 2014, **26**, 1393; (*g*) A. Zevalkink, Y. Takagiwa, K. Kitahara, K. Kimura and G. J. Snyder, *Dalton Trans.*, 2014, **43**, 4720.

9 (*a*) S. Chen and Z. F. Ren, *Mater. Today*, 2013, **16**, 387; (*b*) W. Xie, A. Weidenkaff, X. F. Tang, Qi. Zhang, S. J. Poon and T. M. Tritt, *Nanomaterials*, 2012, **2**, 379; (*c*) J. W. G. Bos and R. A. Downie, *J. Phys.: Condens. Matter*, 2014, **26**, 433201; (*d*) S. J. Poon, D. Wu, S. Zhu, W. Xie, T. M. Tritt, P. Thomas and R. Venkatasubramanian, *J. Mater. Res.*, 2011, **26**, 2795.

10 (*a*) X. Yan, G. Joshi, W. S. Liu, Y. C. Lan, H. Wang, S. Lee, J. W. Simonson, S. J. Poon, T. M. Tritt, G. Chen and Z. F. Ren, *Nano Lett.*, 2011, **11**, 556; (*b*) E. Rausch, B. Balke, S. Ouardi and C. Felser, *Phys. Chem. Chem. Phys.*, 2014, **16**, 25258–25262; (*c*) X. Yan, W. Liu, S. Chen, H. Wang, Q. Zhang, G. Chen and Z. F. Ren, *Adv. Energy Mater.*, 2013, **3**, 1195; (*d*) C. Fu, T. J. Zhu, Y. Pei, H. Xie, H. Wang, G. J. Snyder, Y. Liu, Y. Liu and X. B. Zhao, *Adv. Energy Mater.*, 2014, DOI: 10.1002/aenm.201400600; (*e*) T. Wu, W. Jiang, X. Li, Y. Zhou and L. D. Chen, *J. Appl. Phys.*, 2007, **102**, 103705; (*f*) X. Yan, W. Liu, H. Wang, S. Chen, J. Shiomi, K. Esfarjani, H. Wang, D. Wang, G. Chen and Z. Ren, *Energy Environ. Sci.*, 2012, **5**, 7543.

11 (*a*) S. Sakurada and N. Shutoh, *Appl. Phys. Lett.*, 2005, **86**, 082105; (*b*) D. K. Misra, A. Bhardwaj and S. Singh, *J. Mater. Chem. A*, 2014, **2**, 11913–11921; (*c*) G. Joshi, X. Yan, H. Wang, W. Liu, G. Chen and Z. F. Ren, *Adv. Energy Mater.*, 2011, **1**, 643; (*d*) S. R. Culp, S. J. Poon, N. Hickman, T. M. Tritt and J. Blumm, *Appl. Phys. Lett.*, 2006, **88**, 042106; (*e*) A. Bhardwaj, D. K. Misra, J. J. Pulikkotil, S. Auluck, A. Dhar and R. C. Budhani, *Appl. Phys. Lett.*, 2012, **101**, 133103; (*f*) C. Yu, T. J. Zhu, R. Z. Shi, Y. Zhang, X. B. Zhao and J. He, *Acta Mater.*, 2009, **57**, 2757; (*g*) Q. Shen, L. Chen, T. Goto, T. Hirai, J. Yang, G. P. Meisner and C. Uher, *Appl. Phys. Lett.*, 2001, **79**, 4165.

12 J. Pierre, R. V. Skolozdra, J. Tobola, S. Kaprzyk, C. Hordequin, M. A. Kouacou, I. Karla, R. Currat and E. Lelievre-Berna, *J. Alloys Compd.*, 1997, **262**, 101–107.

13 J. Tobola and J. Pierre, *J. Alloys Compd.*, 2000, **296**, 243–252.

14 S. W. Kim, Y. Kimura and Y. Mishima, *Intermetallics*, 2007, **15**, 349–356.

15 E. Quarez, K.-F. Hsu, R. Pcionek, N. Frangis, E. K. Polychroniadis and M. G. Kanatzidis, *J. Am. Chem. Soc.*, 2005, **127**, 9177.

16 P. F. P. Poudeu, J. D'Angelo, H. J. Kong, A. Downey, J. L. Short, R. Pcionek, T. P. Hogan, C. Uher and M. G. Kanatzidis, *J. Am. Chem. Soc.*, 2006, **128**, 14347.

17 P. F. P. Poudeu, J. D'Angelo, A. D. Downey, J. L. Short, T. P. Hogan and M. G. Kanatzidis, *Angew. Chem., Int. Ed.*, 2006, **45**, 3835.

18 J. Androulakis, K. F. Hsu, R. Pcionek, H. Kong, C. Uher, J. J. Dangelo, A. Downey, T. Hogan and M. G. Kanatzidis, *Adv. Mater.*, 2006, **18**, 1170.

19 J. R. Sootsman, R. J. Pcionek, H. J. Kong, C. Uher and M. G. Kanatzidis, *Chem. Mater.*, 2006, **18**, 4993.

20 A. F. Ioffe, *Semiconductor Thermoelements and Thermoelectric Cooling_Infosearch*, London, 1957.

21 M. G. Kanatzidis, *Acc. Chem. Res.*, 2005, **38**, 359.

22 G. S. Nolas, J. Poon and M. Kanatzidis, *MRS Bull.*, 2006, **31**, 199.

23 W. Kim, J. Zide, A. Gossard, D. Klenov, S. Stemmer, A. Shakouri and A. Majumdar, *Phys. Rev. Lett.*, 2006, **96**, 045901.

24 D. Li, S. T. Huxtable, A. R. Abramson and A. Majumdar, *J. Heat Transfer*, 2005, **127**, 108.

25 A. Majumdar, *Science*, 2004, **303**, 777.

26 L. D. Hicks and M. S. Dresselhaus, *Phys. Rev. B: Condens. Matter*, 1993, **47**, 12727.

27 R. A. Downie, D. A. MacLaren and J.-W. G. Bos, *J. Mater. Chem. A*, 2014, **2**, 6107.

28 R. A. Downie, D. A. MacLaren, R. I. Smith and J.-W. G. Bos, *Chem. Commun.*, 2013, **49**, 4184.

29 X. Y. Huang, Z. Xu and L. D. Chen, *Solid State Commun.*, 2004, **130**, 181.

30 L. D. Chen, X. Y. Huang, M. Zhou, X. Shi and W. B. Zhang, *J. Appl. Phys.*, 2006, **99**, 064305.

31 S. J. Poon, D. Wu, S. Zhu, W. Xie, T. M. Tritt, P. Thomas and R. Venkatasubramanian, *J. Mater. Res.*, 2011, **26**, 2795.

32 X. Y. Huang, Z. Xu, L. D. Chen and X. F. Tang, *Key Eng. Mater.*, 2003, **249**, 79.

33 D. K. Misra, J. P. A. Makongo, P. Sahoo, M. R. Shabetai, P. Paudel, K. L. Stokes and P. F. P. Poudeu, *Sci. Adv. Mater.*, 2011, **3**, 607.

34 X. Y. Huang, L. D. Chen, X. Shi, M. Zhou and Z. Xu, *Key Eng. Mater.*, 2005, **280**, 385.

35 R. Yaqub, P. Sahoo, J. P. A. Makongo, N. Takas, P. F. P. Poudeu and K. L. Stokes, *Sci. Adv. Mater.*, 2011, **3**, 633.

36 D. K. Misra, J. P. A. Makongo, M. R. Shabetai, G. S. Chaubey, J. Wiley, K. L. Stokes and P. F. P. Poudeu, *MRS Spring Meeting*, 2010, vol. 1267, 1267-DD06-12.

37 J. R. Sootsman, J. He, V. P. Dravid, S. Ballikaya, D. Vermeulen, C. Uher and M. G. Kanatzidis, *Chem. Mater.*, 2010, **22**, 869–875.
38 J. Q. He, A. Gueguen, J. R. Sootsman, J. C. Zheng, L. J. Wu, Y. M. Zhu, M. G. Kanatzidis and V. P. Dravid, *J. Am. Chem. Soc.*, 2009, **131**, 17828.
39 J. R. Sootsman, J. Q. He, V. P. Dravid, C. P. Li, C. Uher and M. G. Kanatzidis, *J. Appl. Phys.*, 2009, **105**, 083718.
40 T. Ikeda, L. A. Collins, V. A. Ravi, F. S. Gascoin, S. M. Haile and G. J. Snyder, *Chem. Mater.*, 2007, **19**, 763.
41 S. N. Girard, J. He, X. Y. Zhou, D. Shoemaker, C. M. Jaworski, C. Uher, V. P. Dravid, J. P. Heremans and M. G. Kanatzidis, *J. Am. Chem. Soc.*, 2011, **133**, 16588.
42 K. W. Jang and D. H. Lee, *Fourteenth International Conference on Thermoelectrics*, IEEE, 1995, p. 108.
43 T. Ikeda, S. M. Haile, V. A. Ravi, H. Azizgolshani, F. Gascoin and G. J. Snyder, *Acta Mater.*, 2007, **55**, 1227.
44 W. K. Liebmann and E. A. Miller, *J. Appl. Phys.*, 1963, **34**, 2653.
45 H. J. Wu, W. J. Foo, S. W. Chen and G. J. Snyder, *Appl. Phys. Lett.*, 2012, **101**, 023107.
46 G. I. Isakov, *Semiconductors*, 2005, **39**, 738.
47 G. I. Isakov, *J. Eng. Phys. Thermophys.*, 2004, **77**, 1062.
48 I. V. Dement'ev and V. V. Leonov, *Inorg. Mater.*, 1988, **24**, 19.
49 V. V. Leonov and Z. K. Gantimurova, *Inorg. Mater.*, 1987, **23**, 1683.
50 V. V. Leonov and Y. E. Spektor, *Inorg. Mater.*, 1980, **16**, 918.
51 V. V. Leonov, *Inorg. Mater.*, 1985, **21**, 265.
52 C. Leyens and M. Peters, *Titanium and titanium alloys: fundamentals and applications*, Weinheim, Wiley-VCH, 2003, vol. 1.
53 D. K. Misra, R. K. Rakshit, M. Singh, P. K. Shukla, K. M. Chaturvedi, B. Sivaiah, B. Gahtori, A. Dhar, S. W. Sohn, W. T. Kim and D. H. Kim, *Mater. Des.*, 2014, **58**, 551.
54 D. K. Misra, S. W. Sohn, H. Gabrisch, W. T. Kim and D. H. Kim, High strength Ti–Fe–(In, Nb) composites with improved plasticity, *Intermetallics*, 2010, **18**, 342.
55 D. Keazler, D. Cahen and J. Lbers, *POLSQ FORTRAN program*, Northwestern University, Evanston, IL, 1984.
56 V. Johnson and K. Lark-Horovitz, *Phys. Rev.*, 1953, **92**, 226.
57 J. Wang, J. K. Carson, M. F. North and D. J. Cleland, *Int. J. Heat Mass Transfer*, 2008, **51**, 2389.
58 C. S. Birkel, J. E. Douglas, B. R. Lettiere, G. Seward, N. Verma, Y. Zhang, T. M. Pollock, R. Seshadri and G. D. Stucky, *Phys. Chem. Chem. Phys.*, 2013, **15**, 6990.
59 H. Kitagawa, M. Wakatsuki, H. Nagaoka, H. Noguchi, Y. Isoda, K. Hasezaki and Y. J. Noda, *J. Phys. Chem. Solids*, 2005, **66**, 1635.
60 C. S. Birkel, W. G. Zeier, J. E. Douglas, B. R. Lettiere, C. E. Mills, G. Seward, A. Birkel, M. L. Snedaker, Y. Zhang, G. J. Snyder, T. M. Pollock, R. Seshadri and G. D. Stucky, *Chem. Mater.*, 2012, **24**, 2558–2565.